Kobe University Repository : Kernel

PDF issue: 2025-12-04

A global system of furrows on Ganymede indicative of their creation in a single impact event

Hirata, Naoyuki
Suetsugu, Ryo
Ohtsuki, Keiji

(Citation)
Icarus,352:113941

(Issue Date)
2020-12

(Resource Type)
journal article

(Version)
Accepted Manuscript

(Rights)
© 2020 Elsevier Inc.
This manuscript version is made available under the CC-BY-NC-ND 4.0 license
http://creativecommons.org/licenses/by-nc-nd/4.0/

(URL)
https://hdl.handle.net/20.500.14094/90007458

KOBE UNIVERSITY

Title

A global system of furrows on Ganymede indicative of their creation in a single impact event

Authors

Naoyuki Hirata[1, *], Ryo Suetsugu[2,3], Keiji Ohtsuki[1]

Affiliation

[1] Graduate School of Science, Kobe University, Rokkodai, Kobe 657-8501, Japan

[2] School of Medicine, University of Occupational and Environmental Health, Iseigaoka, Yahata, Kitakyushu, 807-8555, Japan

[3] National Institute of Technology, Oshima College, Suo-Oshima, Yamaguchi, 742-2193, Japan

[*] Corresponding Author Email address: hirata@tiger.kobe-u.ac.jp

Proposed Running Head: Furrows on Ganymede

Editorial Correspondence to:
Dr. Naoyuki Hirata
Kobe University
Rokkodai 1-1 657-8501
Tel/Fax +81-7-8803-6566
Email: hirata@tiger.kobe-u.ac.jp

Key Words
Ganymede
Impact processes
Geological processes
Cratering

Highlight

■ We studied the global distribution of ancient tectonic troughs, furrows on Ganymede

■ We found that furrows used to be a global-scale multi-ring structure.

■ If it is impact origin, an 150-km radius impactor is plausible

Abstract

Furrows are a concentric system of tectonic troughs, and are the oldest recognizable surface feature on Ganymede. We analyzed the distribution of furrows utilizing Voyager and Galileo images and found that furrows over Ganymede's surface are part of a global concentric circular structure. If this multi-ring structure is impact origin, this is the largest impact structure identified so far in the solar system. Deviations of the shapes of the furrows from the concentricity are small everywhere, which implies that the relative location of the blocks of the dark terrains over the entire surface of Ganymede has not changed appreciably even during formation of the bright terrains. The estimate of the impactor size is difficult, but an 150km-radius impactor is consistent with the observed properties of furrows. The furrow-forming impact should have significant effects on the satellite's geological and internal evolution, which are expected to be confirmed by future explorations of Jupiter's icy moons, such as the JUICE (Jupiter Icy moon Explorer) or Europa Clipper mission.

1. Introduction

Several spacecraft such as Voyager and Galileo spacecraft and ground-based observations revealed Ganymede's remarkable properties. One of the most notable surface structures on Ganymede is a concentric system of tectonic troughs, termed furrows (Fig. 1AB). Furrows exist only on geologically old terrains, termed dark terrains. The dark terrains, consisting of 33-34 % of Ganymede's total surface, are heavily cratered and well preserve many ancient craters, as on Callisto (Frieden and Swindell, 1976; Pappalardo et al., 2004; Passey and Shoemaker, 1982; Shoemaker and Wolfe, 1982; Smith et al., 1979a; Smith et al., 1979b). Because furrows are crosscut by any recognizable impact craters exceeding 10 km in diameter, they are regarded as the oldest recognizable surface features on Ganymede (Passey and Shoemaker, 1982). The rest of Ganymede's surface, termed bright terrains, is young terrains that have numerous tectonic features called grooves and lack furrows.

It was proposed that some of the furrows are fragments of multi-ring impact basin structures similar to the Valhalla or Asgard basins on Callisto (Fig 1C), which are thought to be formed by collapse of a crater basin when the excavation depth is comparable to the thickness of the lithosphere of the satellite (McKinnon and Melosh, 1980; Melosh, 1982; Smith et al., 1979a). According to Voyager-era studies, the largest one exists across Galileo Regio and Marius Regio (so-called the Galileo-Marius furrow system) and it has at least hemispherical scale (Schenk and McKinnon, 1987; Zuber and Parmentier, 1984). On the other hand, Voyager images did not cover all of

63 the dark terrain blocks, such as Galileo, Perrine, or Nicholson Regio.
64 Therefore, they do not constrain the scale of Galileo-Marius system. Galileo
65 images covered the regions not imaged by Voyagers and showed that the
66 dark terrain is ubiquitously distributed over the surface of Ganymede and
67 most of them have furrows. However, there are still some areas of dark
68 terrain that are not sufficiently imaged by either mission. For example, few
69 furrows have been found in Melotte Regio, which is presumably because the
70 resolution, illumination, and/or emission of images were not suitable for
71 detecting furrows yet. Future remote-sensing observations may find many
72 more furrows in the dark terrains.

73 In the present work, first we reanalyze the distribution of furrows
74 utilizing both Voyager and Galileo images, and update our knowledge about
75 the scale of this structure (Section 2). We show that this is a structure not in
76 a hemispherical scale but in a global scale, and that it would have been
77 formed by a single large impact. In addition, we estimate the impactor size
78 based on the model of the scale of furrows and numerical simulation (Section
79 3). We discuss implications of our findings for the evolution of the satellite in
80 Section 4, and our conclusions are summarized in Section 5.

81

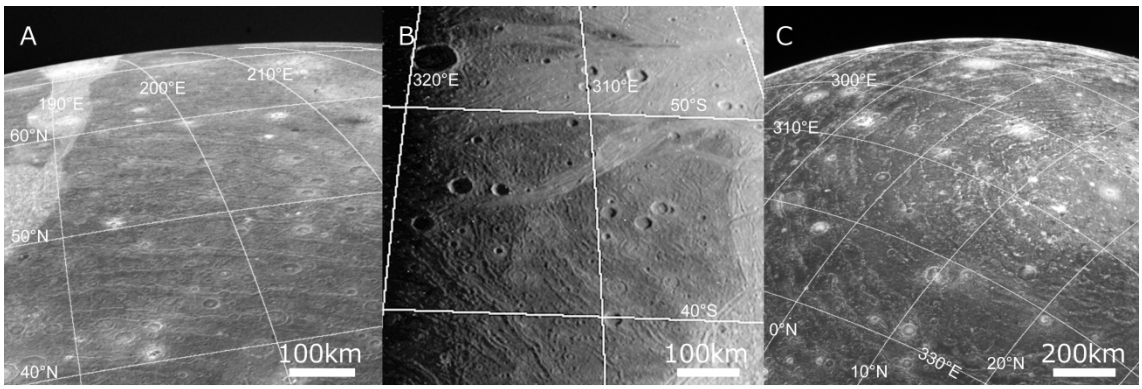

82

Fig. 1. Furrows on Ganymede and the Valhalla ring system on Callisto. (A) A concentric system of tectonic troughs in Galileo Regio of Ganymede, termed furrows (C2063641). (B) A parallel system of furrows in Nicholson Regio of Ganymede (s0401701078), which are one of the furrows newly identified from the Galileo images. Although this region was imaged by Voyagers, the lighting and emission angles of the Voyager images were not suitable for detecting furrows. (C) Valhalla basin on Callisto and its multi-ring system (C1642151).

2. The scale of the furrow system

2.1. Previous studies

The Voyager 1 spacecraft has imaged the sub-jovian hemisphere of Ganymede at a resolution of up to 1.0 km/pixel and Voyager 2 has imaged the anti-jovian hemisphere at a resolution of up to 500 m/pixel. Utilizing these images, furrows are identified in Galileo, Marius, Barnard Regio, the northeastern portion of Perrine Regio, and the eastern portion of Nicholson Regio (e.g. Schenk and McKinnon, 1987; Zuber and Parmentier, 1984). Examination of Voyager images shows that the largest furrow system have a concentric patterns centered at 20°S 180°W across Galileo Regio and Marius Regio, whose scale is at least hemispherical (Fig. 2A) (Schenk and McKinnon, 1987; Zuber and Parmentier, 1984). Because of poor visibility of Voyager images for some area, the scale of this furrow system was uncertain.

The Galileo spacecraft has imaged many portions at moderate resolution (~ 0.8-3.6 km/pixel) during the six close encounters (Pappalardo et

al., 2004). Galileo has imaged many of the dark terrain not resolved by Voyagers. The global geologic map of Ganymede, representing a synthesis of our understanding of Ganymede geology after the conclusion of the Galileo mission, has been published (Collins et al., 2013). Collins et al. (2013) mapped newly-identified furrows in far eastern Galileo Regio, western portion of Perrine Regio, Melotte Regio, the western portion of Nicholson Regio, and unnamed blocks near Ta-urt craters, although the distribution of the furrows is not discussed then.

2.2. Our observation

We utilized Voyager/Galileo images, a global mosaic (U.S. Geological Survey, 2003), and two previous measurements of furrows (Collins et al., 2013; Schenk and McKinnon, 1987), and analyzed the distribution of furrows on Ganymede. We used ISIS3 software produced by the U.S. Geological Survey for both map projections and radio-metrically calibrations. We did not add new furrows in this work. We developed azimuthal equidistant projection maps centered at 20°S 180°W (Fig. 2A), and its exactly opposite hemisphere (Fig 2B). As shown in Fig. 2A, we confirmed that the Galileo-Marius furrow system is aligned in concentric circles centered at a single point, 20°S 180°W. Interestingly, we found that not only furrows in Galileo and Marius Regio but also ones even on the opposite hemisphere are aligned in concentric circles centered at the single point. Although previous works estimated that the system has at least a hemispherical scale (Schenk and McKinnon, 1987), we noticed that furrows over Ganymede form a global

131 concentric system and Galileo-Marius system is a part of the global system.
132 In other words, the scale of the Galileo-Marius furrow system is much
133 greater than previously supposed. Although the dark terrain remained in
134 only one-third of the current surface, our finding indicates that Ganymede
135 used to have a global-scale multi-ring system formed by a single event before
136 the formation of the bright terrain. If these furrows are impact origin, this is
137 the largest impact structure identified so far in the solar system. In order to
138 see the deviation of the shapes of the furrows from the concentricity, we
139 developed an oblique simple cylindrical projection (Fig. 3 and 4). Fig. 3 shows
140 the dark terrain projected on the oblique simple cylinder, and the vertical
141 direction indicates the equidistance from the center. Fig. 4 shows clops of
142 transects of the dark terrains shown in Fig. 3A. Figs. 3 and 4 indicate that
143 the furrows seem to be aligned in the horizontal direction everywhere.

144 In order to assess the above arguments quantitatively, we
145 geometrically analyzed the furrow system over Ganymede following the
146 method of Schenk and McKinnon (1987). The details are described in
147 Appendix A. As a result, we estimated the geometric center of the furrow
148 system to be 21.3°S 179.4°W using furrows in Galileo and Marius Regio and
149 22.9°S 178.4°W using furrows over Ganymede, respectively. These geometric
150 centers obtained in the present work are consistent with the one obtained by
151 Schenk and McKinnon (1987). Furthermore, we calculated the deviation
152 from concentricity of each furrow segment and made its histograms,
153 assuming the center to be 21.3°S 179.4°W (Fig. 5). The histograms for the
154 furrow system over Ganymede showed a sharp peak at 0-5° deviation from

155 concentricity, with 85% of the ring segments aligned within 30° of
156 concentricity (Fig. 5a). According to Schenk and McKinnon (1987), the
157 histogram for Valhalla ring system showed a sharp peak at 0-10° deviation
158 from concentricity, with 90% of the ring segments aligned within 30° of
159 concentricity. Thus, the concentricity of the furrow system over Ganymede
160 was found to be comparable to that of Valhalla ring system. Note that the
161 histograms for Ganymede's furrow system did not exclude radial and
162 sub-radial furrows, but ones for Valhalla ring system done by Schenk and
163 McKinnon (1987) excluded them. Similar plots for furrows in the opposite
164 hemisphere (Nicholson, Perrine, and Melotte Regios) also showed a sharp
165 peak at 0-10° deviation from concentricity, with 90% of the ring segments
166 aligned within 30° of concentricity (Figs. 5b and 5c). Therefore, the
167 concentricity of the furrow system over Ganymede is sufficiently small to be
168 regarded as a single concentric circle system. It has been proposed that
169 furrows lying partly in Galileo Regio shown in the plate G5 in Fig. 3 (and Fig.
170 4F) form a distinct small multi-ring system (Prockter et al., 2002). However,
171 this G5 system is also sufficiently aligned with the global-scale furrow
172 system (Fig. 5d), and therefore, it is possible that the G5 system could be
173 regarded as a part of the global-scale furrow system (this does not mean that
174 the G5 system is not distinct multi-ring system).

175 It is known that Marius Regio (especially, the region within the
176 colatitude of 30° from 20°S 180°W) has few furrows (Fig. 6) (Schenk and
177 McKinnon, 1987; Zuber and Parmentier, 1984). The region within 30 degrees
178 from the center of the above furrow system (r < 1380 km, where r is the

179 radial distance from the center on the satellite's surface) may be the
180 structure corresponding to the central zone without trough or ridge of the
181 Valhalla basin (r < 360 km). This furrow system extends in Barnard Regio
182 (the region from the colatitude 163 to 170 degree), which implies that the
183 furrow system on Ganymede has the extent of 1380 km < r < 7800 km.
184 Unlike the Valhalla ring system, the furrow system of Ganymede does not
185 have either obvious ridged zone or outward-facing normal faults in any dark
186 terrains, which has been already pointed out by McKinnon and Parmentier
187 (1986) based on Voyager images, and our update based on Galileo images has
188 confirmed it again.

189 There is a possibility that a true impact site is not the Marius side
190 (20°S 180°W) but Barnard side (20°N 0°W). At the moment, we cannot argue
191 conclusively which side is the true center. That said, furrows on the Marius
192 side are typically much more obvious than those in the Barnard side. Also, if
193 the true center is on the Barnard side, the central region without furrows is
194 too small. Therefore, in this work, we assume that the true center of the
195 system is on the Marius side.

196 This implies that the relative locations of the blocks of the dark
197 terrains did not change appreciably. Previous work shows that deviations of
198 the shapes of the furrows in Marius Regio and Galileo Regio from the
199 concentricity are small, and therefore, lateral movement of each dark terrain
200 block does not occur between Marius Regio and Galileo Regio (Schenk and
201 McKinnon, 1987). Our observation indicates that relative locations of each
202 dark terrain block over the entire surface of Ganymede (not only Marius and

Galileo but also Perrine Melotte, Nicholson, and Barnard Regio) have been unmodified since the formation of the furrows, despite of their great distances. We verified quantitatively how large lateral movement between each dark terrain block can be detected by the concentricity of furrows. As an example, we shifted the western portion of Nicholson Regio (N2 in Fig. 3) slightly, and examined how the histogram in Fig. 5c changes. Results are shown in Fig. 7 (see Appendix A). In the case of 10° movement, the majority of the deviation was within 20 degrees, but the peak positions were slightly shifted. In the case of 20° movement, the peak positions were shifted or separated. In the case of 30° movement, the histogram no longer followed a normal distribution. Note that the original histogram (Fig. 5c) showed a more ideal normal distribution curve peaked at zero degree than these 15 examples shown in Fig. 7. Therefore, it is likely that the lateral movement of the relative position between Nicholson and Galileo-Marius system would be 20 degrees at maximum (this corresponds to 920 km on Ganymede).

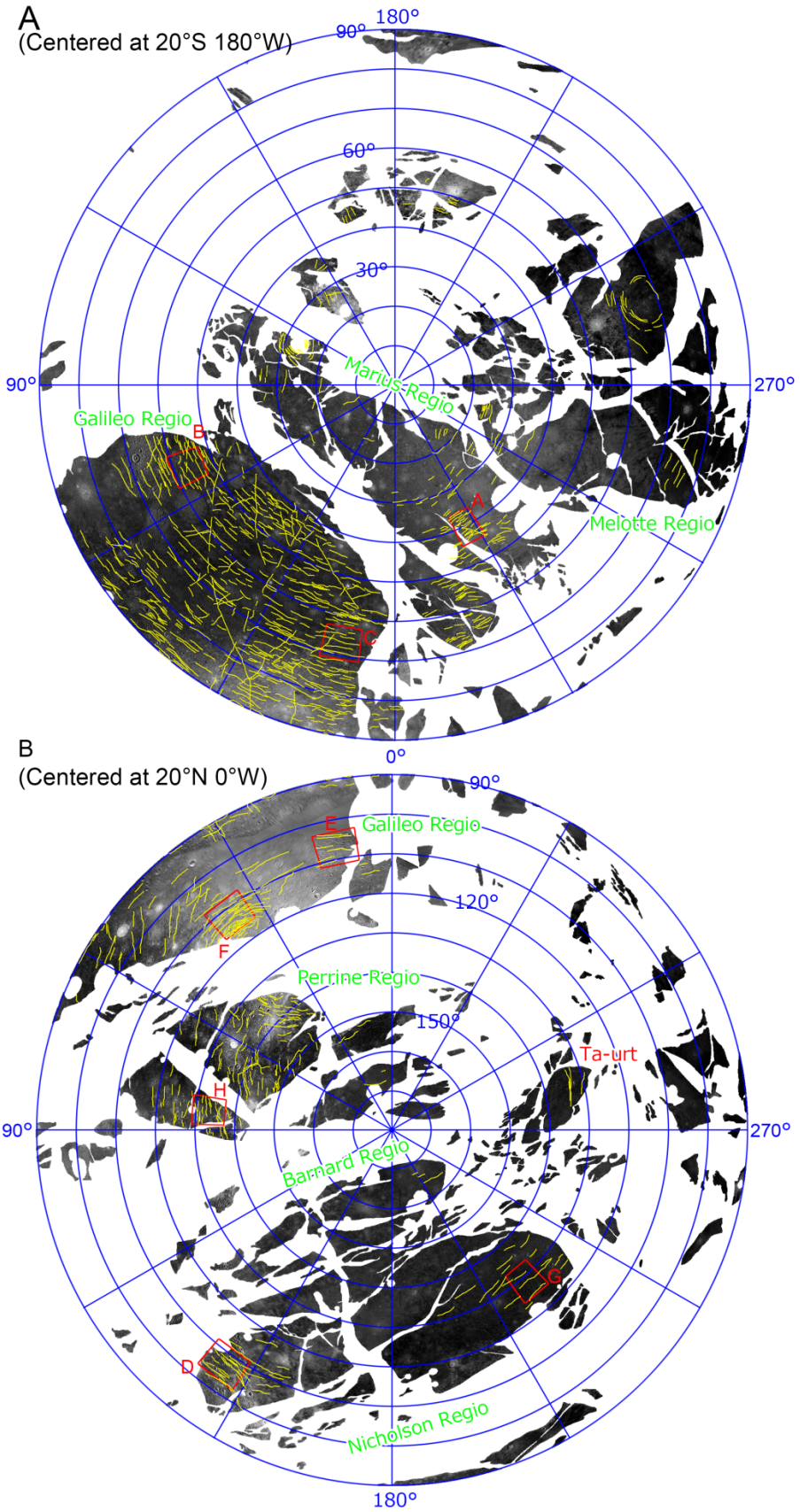
A
(Centered at 20°S 180°W)
180°
90°
60°
30°
90°
270°
Galileo Regio
Marius Regio
Melotte Regio
B
C
0°
B
(Centered at 20°N 0°W)
90°
E
Galileo Regio
120°
F
Perrine Regio
150°
Ta-urt
H
90°
270°
Barnard Regio
G
D
Nicholson Regio
180°

219

220 **Fig. 2.** Distribution of furrows (yellow lines) projected in azimuthal
221 equidistant map centered at 20°S 180°W (plate A) and its exactly opposite
222 point, 20°N, 0°W (plate B). White regions indicate the bright terrains. The
223 distributions of the dark terrain and furrows are from Collins et al. (2013)
224 and Schenk and McKinnon (1987). Red rectangles show the location of each
225 plate in Fig. 4.
226

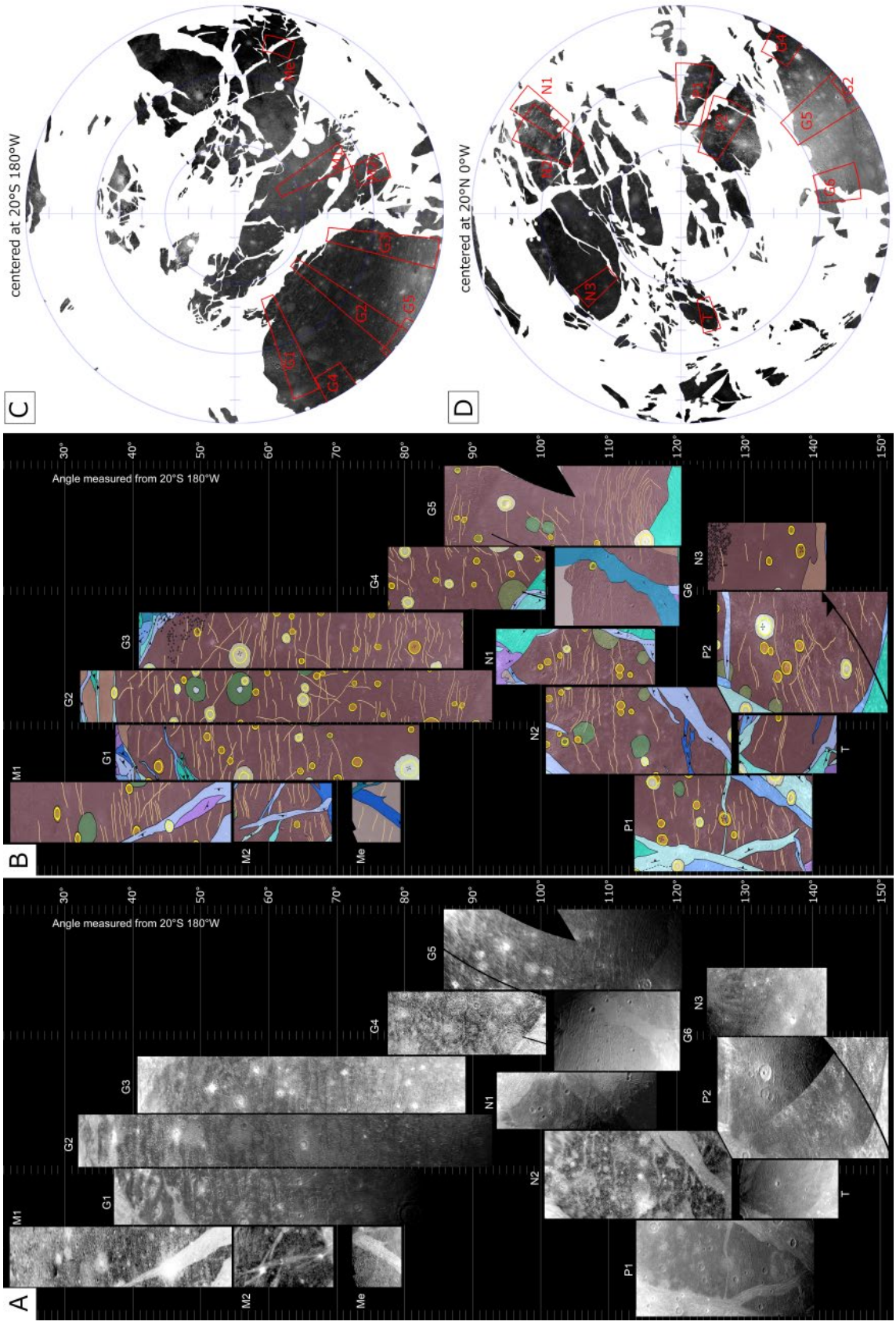
A
B
C
D
Angle measured from 20°S 180°W
centered at 20°S 180°W
centered at 20°N 0°W
M1
M2
Me
G1
G2
G3
G4
G5
G6
N1
N2
N3
P1
P2
T

227

Fig. 3. Transects of the dark terrain of Ganymede along a radial direction from 20°S 180°W to its antipodal point. Vertical axes in plate (A) and (B) represent the colatitude measured from 20°S 180°W. Note that 10° is equivalent to 460 km. Maps in (A) and (B) are shown in oblique simple cylindrical projection poled at 20°S 180°W. Plate (B) is modified from the global geologic map (Collins et al., 2013). Yellow lines and brown areas mean the furrows and the dark terrains identified by Collins et al. (2013). The location of each transect is shown in (C) and (D), which are the projected on the azimuthal equidistant maps centered at 20°S 180°W and its exactly opposite point, 20°N 0°W, respectively. The original-sized image of this figure is uploaded as supplementary Figure S1.

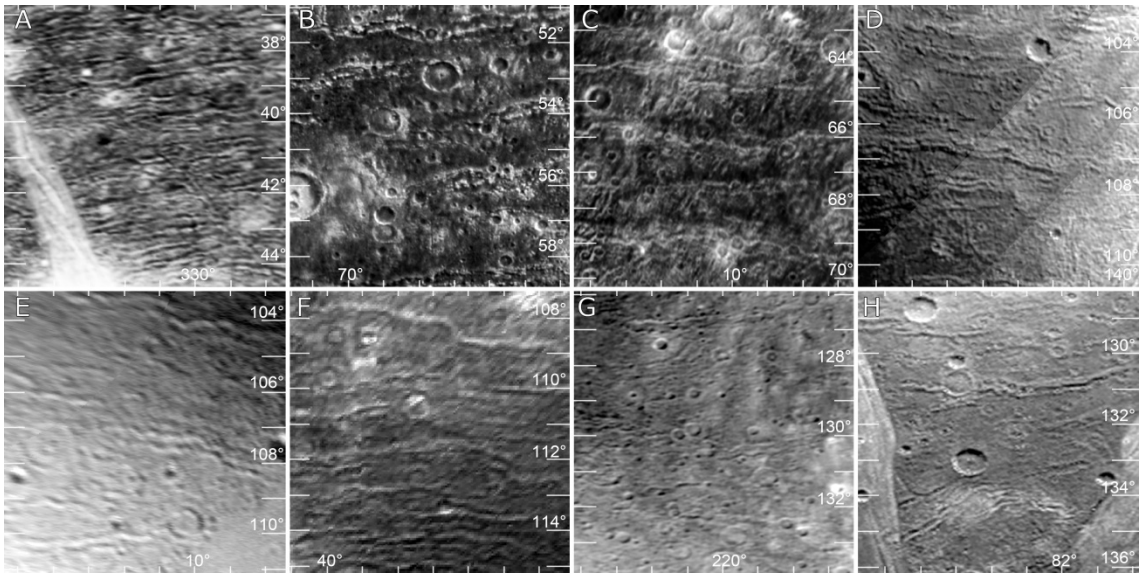

Fig. 4. Close up views of the furrows. Vertical axis represents the colatitude measured from 20°S 180°W. The oblique projection is utilized for this image, and the horizontal axis represents longitude of the oblique simple cylinder. In this figure, the fact that furrows are aligned with the horizontal direction means that they are aligned with concentric circles centered at 20°S 180°W. These images shows Marius Regio (A), Galileo Regio (B, C, E, F), Nicholson Regio (D, G), and Perrine Regio (H), respectively. The detailed locations of each plate are shown in red rectangles of Fig. 2. The appearance of the

249 furrows in each plate (especially, BCDEFH) is similar to each other despite of
250 great difference in their distance, which indicates all have a same origin.
251

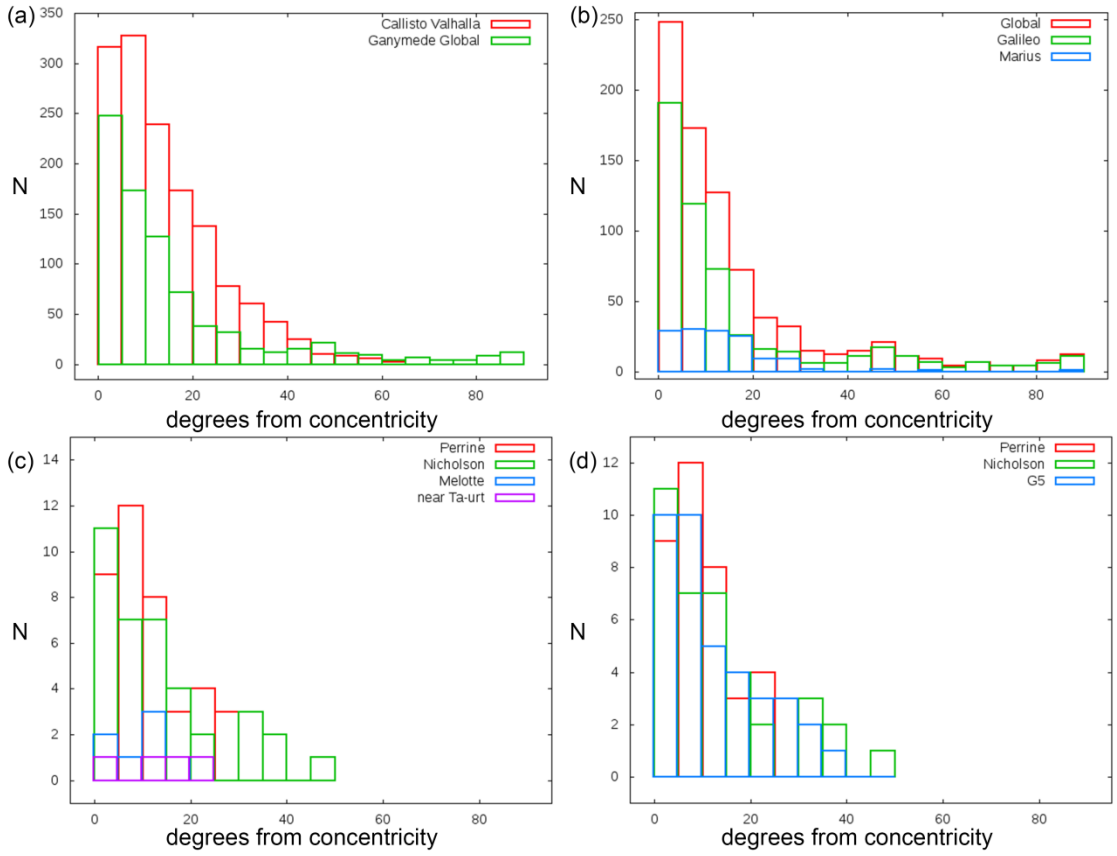

252

253 **Figure 5.** Histograms of the deviation from concentricity (angle of
254 intersection between furrow segments and concentric circles centered at
255 21.3°S 179.4°W). Vertical axis means the number of furrow segments and
256 horizontal axis the degree from concentricity (0° means segments are aligned
257 with concentric circles, while 90° means those are radial to them). Histogram
258 for (a) Valhalla ring system from Schenk and McKinnon (1987) and
259 Ganymede's furrow system over Ganymede from our measurement, (b)
260 Ganymede's furrow system over Ganymede, in Galileo Regio, and in Marius

Regio, (c) for Perrine, Nicholson, Melotte, and unnamed blocks of the dark terrains near Ta-urt crater, and (d) for the G5 small multi-ring system. See also Appendix A.

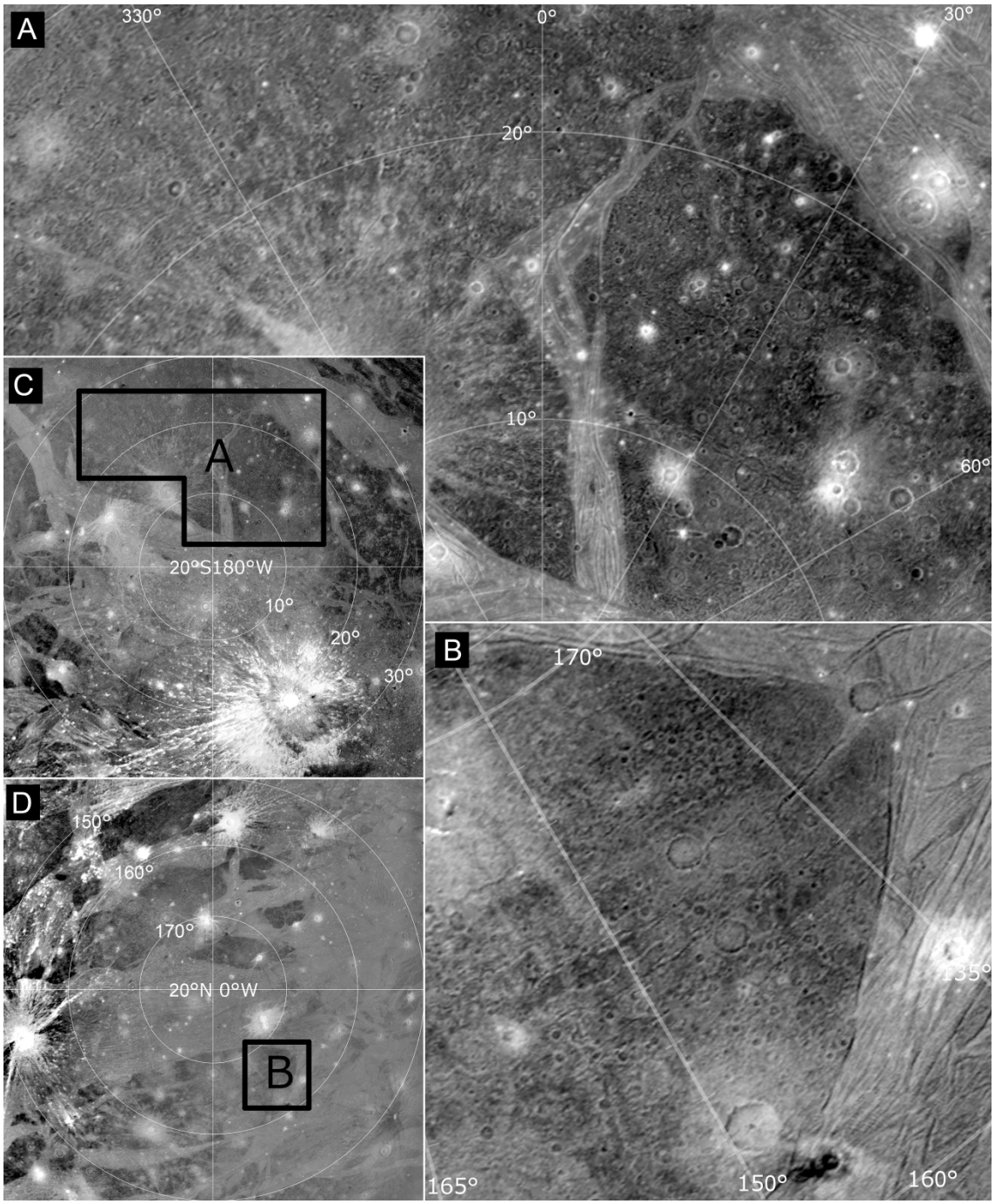

Fig. 6. (A) Close up view of the dark terrains near 20°S 180°W (Marius

267 Regio). (B) That near 20°N 0°W (Barnard Regio). (C) and (D) show the
268 locations of (A) and (B).
269

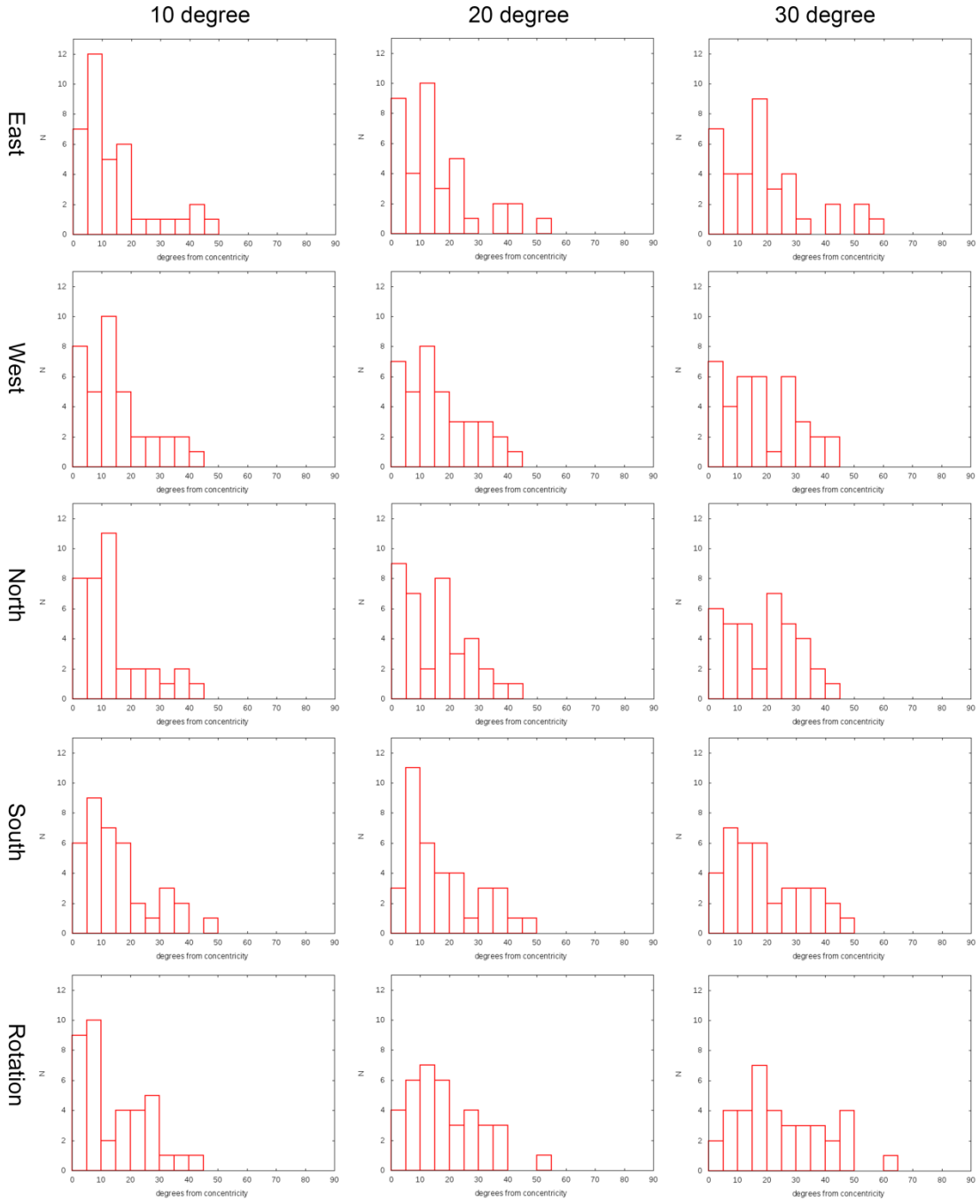

270

271 **Figure 7.** The histogram of the deviation from concentricity between furrow
272 segments in Nicholson Regio that were moved slightly away from its original

location. We show 15 examples: 10°, 20°, and 30° movement toward north, south, west, and east and 10°, 20°, and 30° rotation at the current location without shift. The original one is shown in Fig. 5c. See also Appendix A.

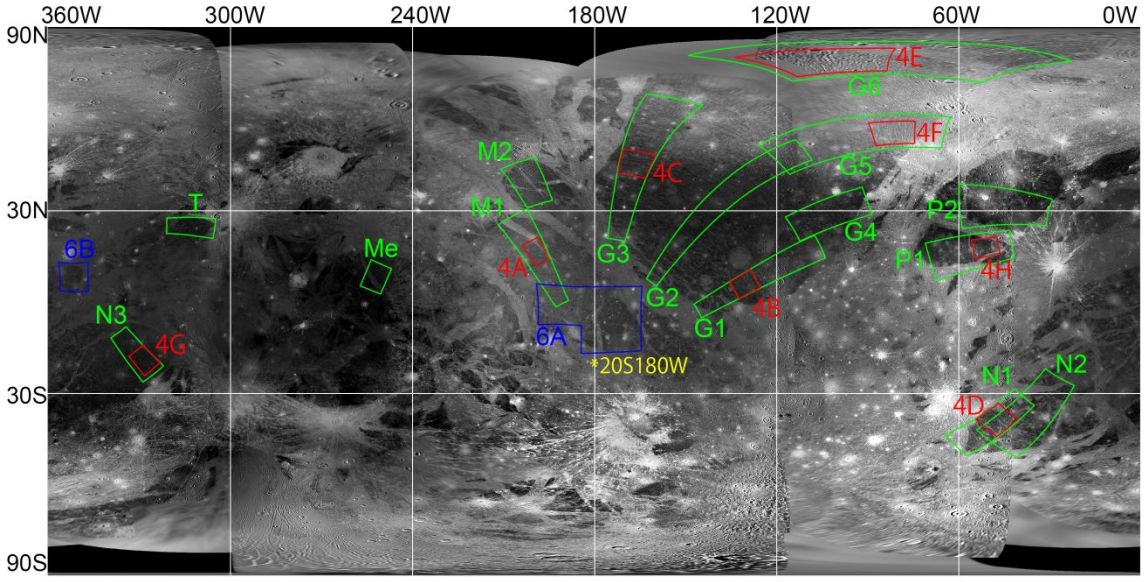

Figure 8. The location of each plate in Figs. 3 (green), 4 (red), and 6 (blue) in simple cylindrical projection map of Ganymede.

3. Impactor size

Estimating the size of the furrow-forming impactor (FFI) is complicated because of the absence of an identifiable clear rim. Absence of clear rim around a seemingly impact-generated structure is not unusual; for example, the Valhalla basin or Asgard basin on Callisto, which are thought to have been formed by an impact, also lacks such a rim (Schenk, 1995). We attempt to estimate the size of FFI based on three considerations: (i) Comparison with Valhalla and Asgard basins on Callisto and palimpsests on

289 Ganymede, (ii) a thin plastic lithosphere model and the extent of furrows,
290 and (iii) numerical simulation.
291
292 **3.1. Comparison with Valhalla and Asgard basins on Callisto and**
293 **palimpsests on Ganymede**
294 Valhalla and Asgard are representative multi-ring impact basins on
295 Callisto. Valhalla basin can be divided into three distinct zones outward from
296 the center: a central smooth zone (r < 360 km, where r means the radial
297 great-circular distance from the center of the basin), an inner ridge and
298 trough zone (360km < r < 950 km), and an outer graben zone (950 km < r <
299 1900 km). Asgard has a central smooth zone (r < 100 km), an inner ridge
300 zone (100 km < r < 400km), and an outer graben zone (400km < r < 940km)
301 (Greeley et al., 2000; Schenk, 1995). It is known that the crater density in the
302 central palimpsest and inner ridge zone of the Valhalla basin is 3.5 times
303 lower than on the adjacent unmodified cratered terrain, while the crater
304 density in the outer graben zone is intermediate between the inner zones and
305 unmodified cratered terrain and apparently increasing linearly outward
306 (Passey and Shoemaker, 1982; Schenk, 1995). The former is due to complete
307 obliteration and tectonic disruption of the original surface, and the latter due
308 to obliteration by continuous ejecta blanket (Schenk, 1995). Although these
309 crater rims collapsed or did not form, these original crater diameters were
310 estimated to be equivalent to 1000 km for Valhalla and 675 km for Asgard
311 based on the mapping of ejecta and secondaries (Schenk and Ridolfi, 2002). If
312 so, we can estimate Valhalla-forming impactor radius to be $R_{imp} \approx 50$ km,

313 using the simple scaling law shown in Eqs. (5) and (6) in Zahnle et al. (2003),
314 15 km/s as the impact velocity onto Callisto (Zahnle et al., 2003), 2000 kg/m^3
315 as the density of the impactor (equivalent to Ceres or Pluto), and 900 kg/m^3
316 as the density of Callisto's crust.

317 A palimpsest is a circular albedo feature around an ancient crater
318 seen on Ganymede and Callisto (Smith et al., 1979a). Palimpsests on
319 Ganymede, such as Memphis Facula, can be divided into four distinct zones
320 outward from the center: the central plains (*cp*) (r < 15% of its palimpsest,
321 where r means the radial great-circular distance from the center of the
322 palimpsest), the unoriented massif facies (*umf*) (15% < r <40%), the
323 concentric massif facies (*cmf*) (40% < r < 70%), and the outer deposits (*od*)
324 (70% < r <100%) (Jones et al. 2003). Beyond the radius of palimpsest, they
325 reported that secondary craters appear. Jones et al. (2003) interpreted these
326 zones to be (*cp*) the central plains to be formed from solidified impact melt
327 and chunks of solid ejecta, (*umf*) a jumbled mass of ejecta located within the
328 transient cavity, (*cmf*) a zone of ejecta-mantled preexisting crust that has
329 been stressed and fractured by the palimpsest-producing impact, and (*od*) a
330 continuous ejecta deposit mantling preexisting terrain. Therefore, Jones et al.
331 (2003) concluded that the original crater rim is the boundary between the
332 *umf* and *cmf* (r= 40% of the scale of palimpsest).

333 Unfortunately, the Voyager or Galileo images do not show any
334 reliable examples of secondaries or ejecta blankets that can be related to the
335 FFI, although some of the craters in the dark terrains on Ganymede may be
336 secondaries. Therefore, we cannot estimate the crater diameter created by

337 the FFI based on counting secondaries. That said, the fact that the furrows
338 are crosscut by all recognizable impact craters may imply that the impact
339 event would have reset Ganymede's surface completely. At least, the scale of
340 the furrow system is roughly 4 times larger than that of the Valhalla ring
341 system; the Valhalla ring system has the extent of 360 km < r < 1900km,
342 while the furrow system on Ganymede has the extent of 1380 km < r <
343 7800km. If the extent of the furrow system corresponds to the *cmf* of
344 Ganymede's palimpsests, the original crater rim would be approximately
345 ~1380km. Therefore, the FFI must be much greater than the impactor
346 forming Valhalla ($R_{imp} \approx 50$ km).
347
348 **3.2. A thin plastic lithosphere model and the extent of furrows**
349 The radial extent of Ganymede's furrows ($r < 7800$ km) also provides
350 an insight into the impactor size. This extent basically depends on the
351 thickness and the strength of the satellite's lithosphere (Melosh, 1982). After
352 (or as soon as) the formation of crater cavity, concentric faulting zone would
353 be formed by tectonics induced by the inward flow of the asthenosphere
354 (Melosh, 1982). We note that it is difficult to examine furrow formation itself
355 by impact simulation due to lack of resolution. Instead, we here utilized a
356 simple physical model known as a thin plastic lithosphere model (Melosh,
357 1982). Based on the model, the extent of faulting zone is a function of a single
358 dimensionless strength parameter,

359 $$\gamma = \frac{\sqrt{3}Sa}{2Yt} ,$$

where γ is dimensionless strength parameter, Y is the strength of lithosphere, a is the transient crater radius, t is the thickness of lithosphere, and S is the constant equal to $(0.05 - 0.1)\rho gd$, where ρ=900 kg/m^3 is the crustal density, g=1.428 m/s^2 is the gravitational acceleration at the surface of Ganymede, and d is the crater depth. Larger dimensionless strength parameter (i.e. larger γ) means thinner or weaker lithosphere, which causes a greater extent of faulting zone, while smaller dimensionless strength parameter (i.e. smaller γ) means thicker or more rigid lithosphere, which forms a compact faulting zone. Following the study for Valhalla (Melosh, 1982), we assume Y = 1 – 10 MPa, S=0.075ρgd, and d=a/5. According to geomorphological analyses of furrows (Nimmo and Pappalardo, 2004), an effective elastic thickness is ~0.5 km and a brittle - ductile transition depth is ~2 to ~3 km. Thus, we assume t= 0.5 – 5 km. Here we examine three cases: thin weak lithosphere model (t=0.5km, Y=1MPa), moderate thickness or weakness lithosphere (t=0.5km, Y=10MPa, or t=5km, Y=1MPa), and thick rigid lithosphere (t=5km, Y=10MPa). Following the model shown in appendix A in Melosh (1982), we calculate the extent of faulting zone as a function of transient crater radius and results are shown in Fig. 9. A transient crater with a radius of a = 800km (this can be generated by R_{imp} = 150 km) can result in a global-scale faulting zone even in the case of the thick and rigid lithosphere. Similarly, if we assume the thin weak lithosphere, a transient crater with a > 300km is sufficient to form a global-scale faulting zone. This radius roughly corresponds to R_{imp} = 50 km (equivalent to an impactor forming Valhalla).

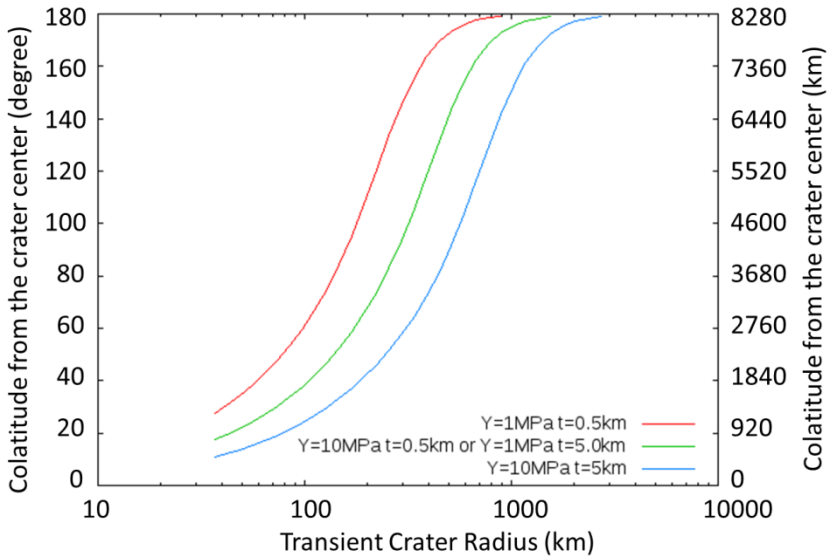

Fig. 9. The extent of faulting zone induced by a given transient crater radius. Vertical axis means the distance from the crater center (in degree or kilometer). Here we assume three cases: thin weak lithosphere with Y=1MPa t = 0.5km, moderate (thick weak or thin rigid) lithosphere with Y=1MPa t= 5km (or Y=10MPa t=0.5km), and thick rigid lithosphere with Y=10MPa t = 5km.

3.3. Numerical Simulation

Instead of aiming at reproducing the furrows themselves, we carried out numerical impact simulation by using shock-physics code iSALE (Amsden et al., 1980; Collins et al., 2004; Wünnemann et al., 2006) to estimate the size of the impactor that can reproduce the scale of the central melt pool formed by the impact. We assume an icy impactor with a radius

400 (R_{imp}) of 150 km or 50km and compare the results of both cases. The detail
401 description for the numerical simulation is given in Appendix B. We found
402 that an impactor with R_{imp} = 50 km generates a transient crater with a
403 radius of 300km and a depth of 250 km, while an impactor with R_{imp} = 150
404 km generates one with a radius of 800km and a depth of 1000 km (Fig. 10).
405 In either case, materials around the impact site become fluidized and any
406 recognizable surface structures such as rims do not form, which is consistent
407 with the properties of the global-scale furrow system. In this simulation, an
408 outward flow from the impact site is generated after the collapse of the
409 central uplift and resurfaces the area around the impact site. In the case of
410 R_{imp} = 150 km, at least the hemispheric region centered at the impact site is
411 modified. On the other hand, an impact with R_{imp} = 50 km would be
412 insufficient for global resurfacing.
413 A numerical simulation to model a Valhalla-like basin using iSALE
414 (Johnson et al., 2013) shows that an impactor with a radius of 50 km can
415 generate a melt pool with a radius of 300 km on Callisto, and it was proposed
416 that the melt pool would be originated from the central bright zone without
417 ridge or trough. Similarly, our simulation shows that an impactor with R_{imp} =
418 150 km can generate a melt pool with a radius of 1000km (here we define a
419 melt pool by a region that experienced a temperature higher than 300K).
420 This agrees with the observed size of the furrow-free central region of Marius
421 Regio. On the other hand, an impactor with R_{imp} = 50 km generates a small
422 melt pool with a radius of 500 km.
423

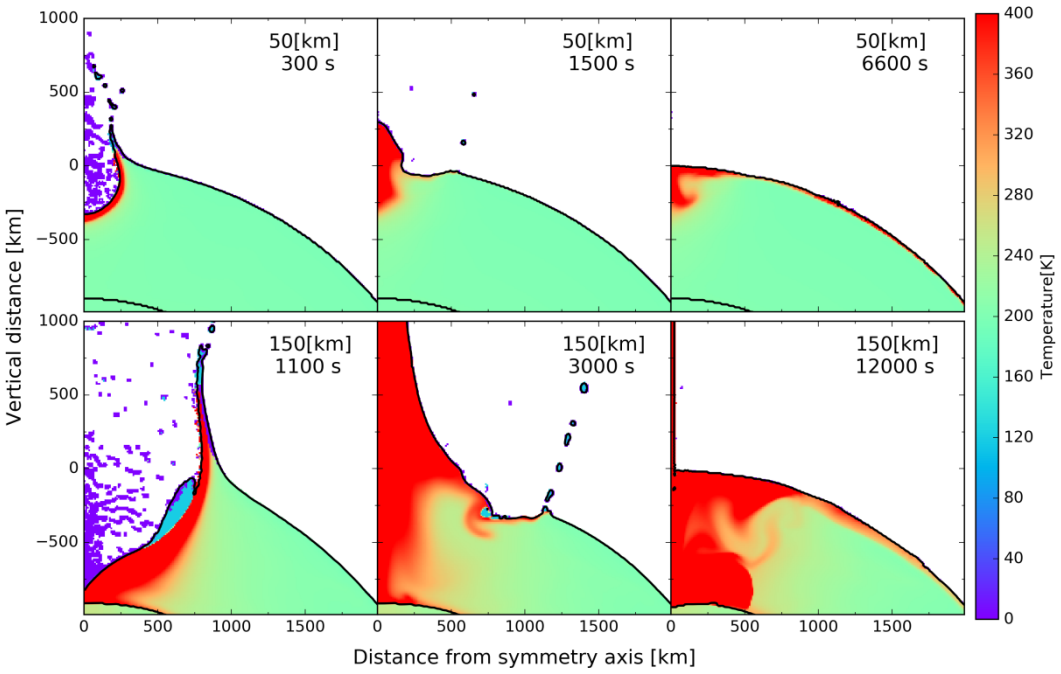

Fig. 10. Time series of simulations of head-on impacts between an impactor and Ganymede. Upper panels show the case of an impactor with a radius of 50 km (see also Movie 1 and 2), and bottom panels show the case of 150 km (Movie 3 and 4).

3.4. Summary

A thin plastic lithosphere model and the extent of furrows show that an impactor with R_{imp} > 50 km is able to form a global-scale faulting zone if Ganymede's lithosphere used to be thin and weak, while R_{imp} = 150 km forms a global-scale faulting zone even in the case of rigid thick lithosphere. Our numerical simulation utilizing iSALE indicates that R_{imp} = 150 km would resurface at least the hemispheric region around its impact site, while R_{imp} =

438 50 km would resurface locally around the impact site. The former is
439 consistent with the view that the furrows are crosscut by any recognizable
440 impact craters, while the latter needs another mechanism to explain the
441 reset of Ganymede's surface. Furthermore, an impactor with R_{imp} = 150 km
442 can generate a melt pool with a radius of 1000km, which could explain
443 furrow-free central region of Marius Regio. Taken all together, we conclude
444 that an impactor with a radius of 150 km is consistent with current
445 properties of the global-scale furrow system. At least, it should be
446 significantly greater than 50 km in radius.
447
448 **4. Discussion and Implication**
449 If furrows are created by an impact, this large impact should have
450 affected the geology of Ganymede significantly. It is known that the crater
451 density in most heavily cratered terrains of Ganymede is slightly lower than
452 that of Callisto (Strom et al., 1981). Such old craters are considered to be
453 formed during the Late Heavy Bombardment (LHB, 4.1~3.8 Ga), according
454 to the so-called Nice model (Gomes et al., 2005). Perhaps, the FFI would have
455 taken place during the LHB, would have reset the crater age of Ganymede,
456 and would be responsible for the difference in the crater densities between
457 Ganymede and Callisto.
458 Our numerical impact simulation for the case of R_{imp} = 150 km (R_{imp}
459 =50 km) demonstrates the generation of a large melt region with a radius of
460 ~1000 km (~500 km). This large melt region would allow the dense material
461 to gravitationally segregate, which generate positive gravity anomaly such

462 as mass concentrations seen on the lunar impact basins. Therefore, we
463 predict that, if our view is correct, positive gravity anomaly with a radius of
464 ~1000 km when R_{imp} = 150 km (or a radius of ~500 km when R_{imp} = 50 km)
465 should exist around 20°S 180°W. This can be tested by future geodetic
466 observations of Ganymede such as the JUICE (Jupiter Icy moon Explorer) or
467 Europa Clipper mission. Interestingly, Ganymede is locked in synchronous
468 rotation and the center of the furrow system coincides with the anti-Jovian
469 longitude (180°W). This is consistent with the existence of large mass
470 anomaly created by the FFI. Also, detailed examination of the topography
471 may find the existence of the circular or radial structure associated with an
472 impact basin, rim crests, or ejecta. At the same time, the question if this
473 furrow system is really impact origin could be also tested by the future
474 geodetic observations. For example, it is proposed that the furrow system can
475 be formed by another mechanism, such as mantle convection (Casacchia and
476 Strom, 1984).

477 The radius of the FFI is still uncertain and it may be smaller or
478 greater than our estimate. If the FFI was twice as large as our estimate, it
479 would have melted about half the volume of Ganymede. The accumulated
480 dense material (iron or silicate) in the large melt region would form a large
481 negatively buoyant mass at the bottom of the pool that stresses the
482 underlying material and rapidly sink toward the satellite's center. This
483 segregation can trigger the whole body differentiation (Tonks and Melosh,
484 1992). In contrast, Callisto does not have evidence of such large impact
485 events. This scenario may explain the so-called Ganymede-Callisto

dichotomy; Ganymede is fully differentiated while Callisto's differentiation is incomplete, despite of the similarity between Ganymede and Callisto in size and composition (Schubert et al., 2004). Note that it is proposed that Ganymede's differentiation are created by slight advantage of (i) radioactive decay and/or (ii) tidal heating, because the silicate mass fraction of Ganymede is a little larger than that of Callisto, and Ganymede is closer to the planet than Callisto (e.g. Schubert et al., 2004). Also, it is proposed that numerous impacts during the late heavy bombardment have been sufficiently energetic to lead to differentiation in Ganymede (Barr and Canup, 2010).

Although our present work demonstrated for the first time that the furrow system of Ganymede was likely created by a single large impact during LHB, it is highly desirable to derive further constraints on the origin of the furrow system from more detailed observations in addition to the geomorphological study done in the present work.

5. Conclusion

We found that almost all of the furrows over Ganymede are aligned in concentric circles centered at 20°S 180°W and the histogram of the degree of concentricity for furrows over Ganymede shows a sharp peak at 0-5° deviation from concentricity, with 85% of the ring segments aligned within 30° of concentricity. This indicates that the scale of the furrow system (so-called the Galileo Marius furrow system) on Ganymede is much greater than previously supposed, and that Ganymede used to have a global-scale

multi-ring impact structure formed by a single impact event. The concentricity of the furrow system seems to suggest that a lateral movement between each dark terrain block is small or not occurred over the entire surface of Ganymede even during the formation of the bright terrains, although the surface of Ganymede has been tectonically modified significantly during formation of the bright terrains. The estimate of the impactor size is difficult, but an 150km-radius impactor is consistent with the properties of the furrow system, even though this estimate includes some uncertainty. If the above estimate is correct, we predict that Ganymede has positive gravity anomaly with a radius of ~1000 km around 20°S 180°W. These could be tested by future observations, such as JUICE or Europa Clipper mission.

Appendix A. Measurements of furrow system

We measured the geometric center of furrows and the deviation from concentricity of each furrow segment. Our measurement of Ganymede's furrow system is almost the same as the method of Schenk and McKinnon (1987). The geometric center of the furrow system was estimated by minimizing the sum of the residuals:

$$\sum_i (R_a - R_b)_i^2 \quad , \text{(A1)}$$

where R_a and R_b were the great-circular distance between the endpoints of the ith furrow segment and the geometric center of the furrow system. In this paper, although the length of each furrow segment varies widely, we did not adopt weighting in each length. The deviation from concentricity of each

534 furrow segment (angle of intersection between furrow segments and
535 concentric circles) was defined by

536 $$\sin^{-1}\left(\frac{R_a - R_b}{A}\right)$$, (A2)

537 where A was the length of each furrow segment (i.e. great-circular distance
538 between R_a and R_b).

539 We obtained R_a, R_b, and A from furrow segments determined by
540 Ganymede's global geologic map (Collins et al., 2013). Collins et al. (2013)
541 identified 906 furrow segments over Ganymede: 532 in Galileo Regio, 161 in
542 Marius, 25 in Melotte, 37 in Nicholson, 128 in Perrine, 4 in unnamed block of
543 the dark terrain near Ta-urt crater, and 19 in the rest of Ganymede. Other
544 than the system centered at 20°S 180°W, some distinct furrow systems exist
545 on the dark terrains, for example, small multi-ring structures centered at
546 28°S 155°W (Marius Regio), 25°S 255°W (Melotte Regio), or 56°N 46°W
547 (Perrine Regio) (e.g. Collins et al., 2013; Schenk and McKinnon, 1987). When
548 we calculated the geometric center, we excluded furrows of these small
549 multi-ring systems. As a result, we obtained the center of the furrow system
550 to be 21.3°S 179.4°W based on furrow segments in Galileo and Marius Regio.
551 Then, we excluded radial furrows (i.e. furrows whose deviation from
552 concentricity is greater than 20°). These geometric centers obtained in the
553 present work are consistent with the one obtained by Schenk and McKinnon
554 (1987), 20.7°S 179.2°W. Similarly, using furrow segments over Ganymede
555 (including Galileo, Marius, Melotte, Nicholson, Perrine Regios, and unnamed
556 block of the dark terrain near Ta-urt crater), we obtained the center of the
557 furrow system to be 22.9°S 178.4°W.

Furthermore, we calculated the deviation from concentricity of each furrow segment and made its histograms, assuming the center to be 21.3°S 179.4°W (Fig. 5). Note that, even if we used any of the above three centers, the histograms hardly changed. In Fig. 7, we excluded the three small multi-ring structures in Marius, Melotte, and Perrine Regios but excluded neither radial furrow systems nor the G5 multi-ring furrow system (furrows lying partly in Galileo Regio shown in G5 in Fig. 3 and Fig. 4F). Histograms for the G5 furrow system was shown in Fig. 5d. In Fig. 5a, as a comparison, we added the case of Valhalla ring system on Callisto obtained by Schenk and McKinnon (1987). Note that Schenk and McKinnon (1987) excluded radial ring segments from this histogram, and therefore it did not include ring segments with large deviation. Histogram for Perrine Regio was made from furrows in southern block of Perrine Regio shown in P1 in Fig. 3 and Fig. 4H, because northern block of Perrine Regio includes many largely-sinuous furrows, which are probably a part of the distinct multi-ring structure.

Next, we attempt to verify quantitatively how large lateral movement between each dark terrain block can be detected by the concentricity of furrows. As an example, we shift the western portion of Nicholson Regio (approximately 40°S 40°W, N2 in Fig. 3) slightly, and see how the histogram in Fig. 5c changes. The movement of the rigid block on a spherical surface can be described as a rotation about a fixed axis known as an Euler pole. The change of the histograms after the movement largely depends on the location of the pole. For example, if the Euler pole of the

582 movement of Nicholson Regio is 20°S 180°W, the histogram of the deviation
583 does not change at all. In this section, we tested 15 simple cases: 10°, 20°,
584 and 30° movement toward north, south, west, and east and 10°, 20°, and 30°
585 right-hand thread rotation at current location without shift. When moving
586 Nicholson toward north, we assumed the Euler pole of the rotation to be 0°N
587 130°W. When rotating Nicholson without shift, we assumed the Euler pole of
588 the rotation to be 40°S 40°W. Then, Rodriguez's rotation formula was used to
589 calculate these movements. The operation that all of furrows are moved by
590 the formula is actually equal to one that the geometric center of 21.3°S
591 179.4°W is moved by the inverse formula. Therefore, we calculated angle of
592 intersection between furrow segments at current location and the concentric
593 circles centered at the center that was moved inversely. The results were
594 shown in Fig. 7.
595
596 **Appendix B. Numerical Method**
597 We use the iSALE-2D shock physics code (Wünnemann et al., 2006),
598 which is an extension of the SALE hydrocode (Amsden et al., 1980). To
599 simulate hypervelocity impact processes in solid materials, SALE was
600 modified to include an elasto-plastic constitutive model, fragmentation
601 models, various equations of state, and multiple materials (Ivanov et al.,
602 1997; Melosh et al., 1992). More recent improvements include a modified
603 strength model (Collins et al., 2004), a porosity compaction model (Collins et
604 al., 2011; Wünnemann et al., 2006) and a dilatancy model (Collins, 2014).
605 We employ the two-dimensional cylindrical coordinate system and

606 perform head-on impact simulations between Ganymede and an impactor.
607 We assume that Ganymede is differentiated into an icy mantle and a rocky
608 core. Its radius and the thickness of the icy mantle are fixed at 2600 km and
609 900 km, respectively (Schubert et al., 2004). We performed simulations with
610 several different sizes of the core, and confirmed that the size of the melt pool
611 does not change significantly. For example, Figure A1 shows the temperature
612 distribution in a coreless Ganymede after the impact. The size of the melt
613 pool was roughly 1000 km, which was consistent with the differentiated
614 Ganymede case (Fig.10). The impactor is assumed to be composed of ice, and
615 its impact velocity is fixed at 20 km/s (Zahnle et al., 2003). We assume an
616 impactor radius (R_{imp}) to be 50 km or 150 km and compare the results of both
617 cases. Following previous works, we use the Tillotson equation of state for ice
618 (Tillotson, 1962) and ANEOS equation of state for dunite (Thompson and
619 Lauson, 1974). The strength and damage model parameters for ice and
620 dunite are listed in Table A1, whose values are used by previous works
621 (Johnson et al., 2016a; Johnson et al., 2016b; Senft and Stewart, 2008). We
622 assume the temperature of the surface and icy mantle of the target to be 120
623 K and 200-210 K, respectively (Nimmo and Pappalardo, 2004; Schubert et al.,
624 2004). We assume the temperature of the impactor to be equal to the surface
625 of Ganymede, 120 K. We also consider the effect of acoustics fluidization
626 using results obtained by impact simulations (Bray et al., 2014). We assume
627 that the angle of impact is perpendicular to the horizon. Note that an oblique
628 impact cannot be simulated in iSALE-2D. Most of grid-based hydrodynamic
629 codes cannot treat the undifferentiated body with the mixture of rock and ice,

630 and therefore, ice/ice impacts have been used to simulate impacts onto
631 undifferentiated bodies. This assumption has been considered to be
632 reasonable because rock particles hardly influence the ice EOS when the size
633 of the rock particle embedded in the ice is small (e.g. Bar and Canup, 2011).

634 Since we aim to evaluate the size of a melt pool after the impact in
635 this impact simulation, we perform numerical integration for a period of time
636 that is sufficiently long for the impact site to become stabilized. When R_{imp} =
637 50 km, the required simulation period is T=5000-10000 s, while it is
638 T=10000-15000 s when R_{imp}=150 km. In order to examine the extent of ejecta
639 blankets, we carry out impact simulation using large computational domain
640 of 7800 km × 13000 km, whose spatial cell size is 10 km. The iSALE-2D
641 supports two types of gravity field model: central gravity and self-gravity.
642 The central gravity model can calculate spatially varying gravity field, which
643 is independent of time. On the other hand, the gravity field by the
644 self-gravity model is calculated from mutual gravity between the
645 computational cells, and is updated periodically (Davison et al., 2012). In
646 this study, the temporal variation of the gravity field can be assumed to be
647 small because the target deformation due to the impact is small. Thus, we
648 apply the central gravity model. Indeed, although we also carried out impact
649 simulations using the self-gravity model, outcomes were almost the same as
650 the case of the central gravity model (Fig. A2).

651

652 **Table A1. iSALE material parameters**

Description	Ice	Dunite
Poisson's ratio	0.33 [*1]	0.25 [*5]

Thermal softening	1.84 *1	1.1 *5
Melting temperature (K)	273.15 *1	1373 *5
Simon A parameter (Pa)	-----	1.52×10^{9} *5
Simon C parameter	-----	4.05 *5
Strength model	ICE *2	ROCK *5
Cohesion (undamaged) (Pa)	1.64×10^{7} *1	5.07×10^{6} *5
Coefficient of internal friction (undamaged)	6.54 *1	1.58 *5
Limiting strength at high pressure (Pa)	1.47×10^{8} *1	3.26×10^{9} *5
Cohesion (damaged) (Pa)	10^{4} *1	10^{4} *5
Coefficient of internal friction (damaged)	0.55 *1	0.63 *5
Limiting strength at high pressure (Pa)	1.47×10^{8} *1	3.26×10^{9} *5
Damage model	COLLINS *6	COLLINS *6
Brittle ductile transition (Pa)	6.89×10^{8} *1	1.23×10^{9} *5
Brittle plastic transition (Pa)	6.99×10^{8} *1	2.35×10^{9} *5
Tensile strength (Pa)	1.7×10^{5} *1	10^{7} *5
Acoustic fluidization model	Block *3	-----
Acoustic fluidization viscosity constant	0.553 (R_{imp}=50km) 0.785 (R_{imp}=150km) *4	-----
Acoustic fluidization decay time constant	45.1 (R_{imp}=50km) 24.9 (R_{imp}=150km) *4	-----

*1 (Johnson et al., 2016b; Senft and Stewart, 2008)

*2 (Collins et al., 2016)

*3 (Ivanov and Kostuchenko, 1997)

*4 (Bray et al., 2014)

*5 (Johnson et al., 2016a)

*6 (Collins et al., 2004)

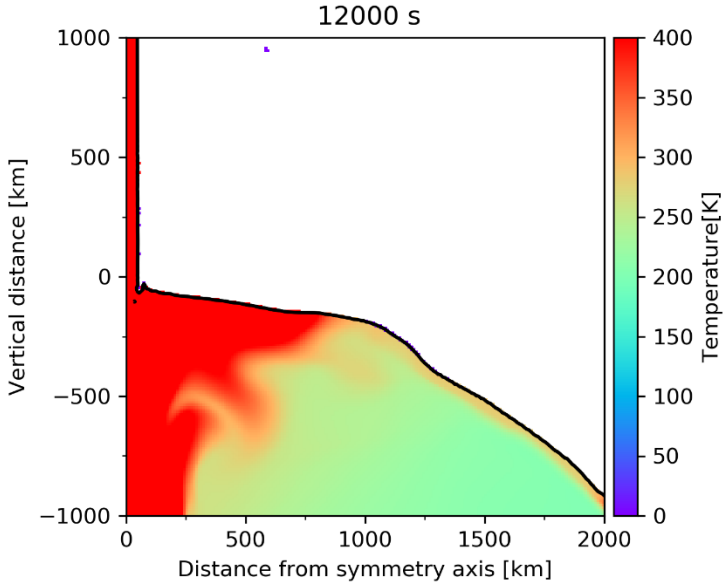

659

660 **Figure A1.** The size of melt pool for the case of coreless Ganymede.

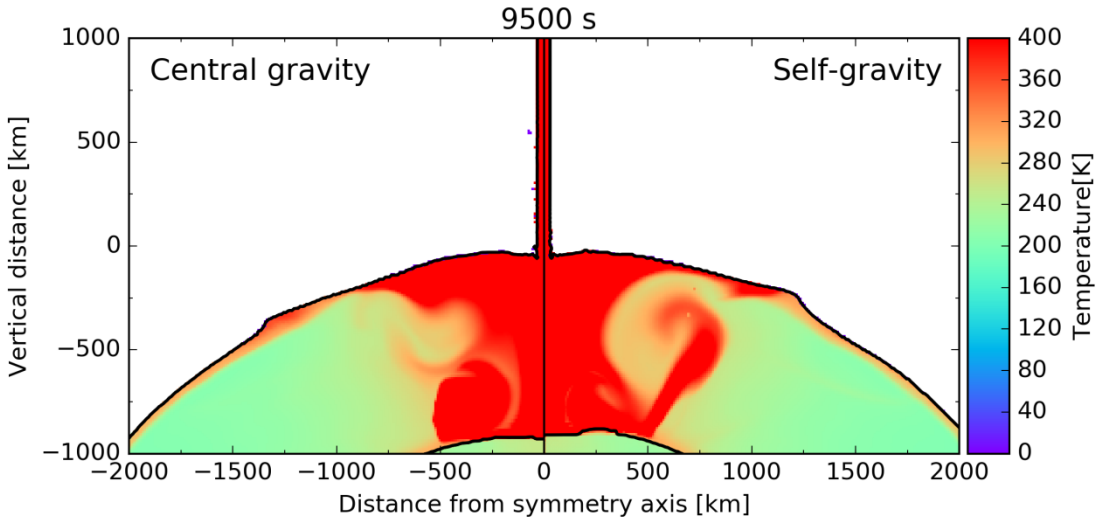

661

662 **Figure A2.** The size of melt pool on central gravity model (left) and

663 self-gravity model (right) in the case of R_{imp}=150 km (see also Movie 5).

664

665 **Acknowledgements**

666 The authors wish to thank Geoffrey Collins for his comments, which

667 significantly tightened the manuscript. This work was partly supported by

JSPS KAKENHI Grant Number JP15H03716 (all), JP19K14787 (R.S.), 20K14538, and 20H04614 (N.H.) and by the Hyogo Science and Technology Association (N.H.). Numerical calculations were in part performed using the PC cluster at the National Astronomical Observatory of Japan. We gratefully acknowledge the developers of iSALE, including Gareth Collins, Kai Wünnemann, Boris Ivanov, H. Jay Melosh, Dirk Elbeshausen, and Thomas Davison.

Supporting information

There are one supplementary figure and five movies. Captions for Figure S1 and Movies are listed below.

Figure S1. The original-sized image of Fig. 3.

Movie 1. The animation of upper panels of Fig. 10.

Movie 2. The entire of Ganymede of Movie 1.

Movie 3. The animation of bottom panels of Fig. 10.

Movie 4. The entire of Ganymede of Movie 3.

Movie 5. The animation of Figure A2.

References

Amsden, A. A., H. M. Ruppel, and C. W. Hirt (1980), SALE: a simplified ALE computer program for fluid flow at all speeds, Los Alamos National Laboratory Report LA-8095 – 1980, Los Alamos, NM.

Barr, A. C., R. M. Canup, (2010), Origin of the Ganymede-Callisto dichotomy by impacts during the late heavy bombardment, *Nature Geoscience 3*, 164.

Bray, V. J., G. S. Collins, J. V. Morgan, H. J. Melosh, and P. M. Schenk (2014), Hydrocode

694 simulation of Ganymede and Europa cratering trends – How thick is Europa's crust?,
695 *Icarus*, *231*, 394-406, doi:https://doi.org/10.1016/j.icarus.2013.12.009.
696 Casacchia, R., and R. G. Strom (1984), Geologic evolution of Galileo Regio, Ganymede,
697 *Journal of Geophysical Research: Solid Earth*, *89*(S02), B419-B428,
698 doi:10.1029/JB089iS02p0B419.
699 Collins, G. C., G. W. Patterson, J. W. Head, R. T. Pappalardo, L. M. Prockter, B. K. Lucchitta,
700 and J. P. Kay (2013), Global geologic map of Ganymede: U.S. Geological Survey
701 Scientific Investigations Map 3237, pamphlet 4 p., 1 sheet, scale 1:15,000,000,
702 http://dx.doi.org/10.3133/sim3237.
703 Collins, G. S. (2014), Numerical simulations of impact crater formation with dilatancy,
704 *Journal of Geophysical Research: Planets*, *119*(12), 2600-2619,
705 doi:doi:10.1002/2014JE004708.
706 Collins, G. S., D. Elbeshausen, K. Wünnemann, T. M. Davison, B. A. Ivanov, and H. J.
707 Melosh (2016), iSALE: A multi-material, multi-rheology shock physics code for
708 simulating impact phenomena in two and three dimensions. iSALE-Dellen manual.
709 Collins, G. S., H. J. Melosh, and K. Wünnemann (2011), Improvements to the ε-α porous
710 compaction model for simulating impacts into high-porosity solar system objects,
711 *International Journal of Impact Engineering*, *38*(6), 434-439,
712 doi:https://doi.org/10.1016/j.ijimpeng.2010.10.013.
713 Collins, G. S., M. H. Jay, and I. B. A. (2004), Modeling damage and deformation in impact
714 simulations, *Meteoritics & Planetary Science*, *39*(2), 217-231,
715 doi:doi:10.1111/j.1945-5100.2004.tb00337.x.
716 Davison, T. M., F. J. Ciesla, and G. S. Collins (2012), Post-impact thermal evolution of porous
717 planetesimals, *Geochimica et Cosmochimica Acta*, *95*, 252-269,
718 doi:https://doi.org/10.1016/j.gca.2012.08.001.
719 Frieden, B. R., and W. Swindell (1976), Restored Pictures of Ganymede, Moon of Jupiter,
720 *Science*, *191*(4233), 1237-1241, doi:10.1126/science.191.4233.1237.
721 Gomes, R., H. F. Levison, K. Tsiganis, and A. Morbidelli (2005), Origin of the cataclysmic
722 Late Heavy Bombardment period of the terrestrial planets, *Nature*, *435*, 466,
723 doi:10.1038/nature03676.
724 Greeley, R., J. E. Klemaszewski, and R. Wagner (2000), Galileo views of the geology of
725 Callisto, *Planetary and Space Science*, *48*(9), 829-853,
726 doi:https://doi.org/10.1016/S0032-0633(00)00050-7.
727 Ivanov, B. A., D. Deniem, and G. Neukum (1997), Implementation of dynamic strength
728 models into 2D hydrocodes: Applications for atmospheric breakup and impact
729 cratering, *International Journal of Impact Engineering*, *20*(1), 411-430,

doi:https://doi.org/10.1016/S0734-743X(97)87511-2.

Ivanov, B., and V. Kostuchenko (1997), Block oscillation model for impact crater collapse, in *28th Lunar and Planetary Science Conference*, Abstract #631, Lunar and Planetary Institute, Houston.

Johnson, B. C., T. J. Bowling, A. J. Trowbridge, and A. M. Freed (2016b), Formation of the Sputnik Planum basin and the thickness of Pluto's subsurface ocean, *Geophysical Research Letters*, *43*(19), 10,068-10,077, doi:doi:10.1002/2016GL070694.

Johnson, B. C., T. J. Bowling, and H. J. Melosh (2013), Formation of Valhalla-Like Multi-Ring Basins, in *44th Lunar and Planetary Science Conference*, Abstract #1302, Lunar and Planetary Institute, Houston.

Johnson, B. C., et al. (2016a), Formation of the Orientale lunar multiring basin, *Science*, *354*(6311), 441-444, doi:10.1126/science.aag0518.

Jones, K. B., J. W. Head III, R. T. Pappalardo, J. M.Moore, (2003), Morphology and origin of palimpsests on Ganymede based on Galileo observations, *Icarus 164(1)*, 197-212.

McKinnon, W. B., and E. Parmentier (1986), Ganymede and Callisto, in *Satellites* (Eds. J. A. Burns and M. S. Matthews), University of Arizona Press, Tucson.

McKinnon, W. B., and H. J. Melosh (1980), Evolution of planetary lithospheres: Evidence from multiringed structures on Ganymede and Callisto, *Icarus*, *44*(2), 454-471, doi:http://dx.doi.org/10.1016/0019-1035(80)90037-8.

Melosh, H. J. (1982), A simple mechanical model of Valhalla Basin, Callisto, *Journal of Geophysical Research: Solid Earth*, *87*(B3), 1880-1890, doi:10.1029/JB087iB03p01880.

Melosh, H. J., E. V. Ryan, and E. Asphaug (1992), Dynamic fragmentation in impacts: Hydrocode simulation of laboratory impacts, *Journal of Geophysical Research: Planets*, *97*(E9), 14735-14759, doi:10.1029/92JE01632.

Nimmo, F., and R. T. Pappalardo (2004), Furrow flexure and ancient heat flux on Ganymede, *Geophysical Research Letters*, *31*(19), L19701, doi:10.1029/2004GL020763.

Pappalardo, R. T., G. C. Collins, J. Head, P. Helfenstein, T. B. McCord, J. M. Moore, L. M. Prockter, P. M. Schenk, and J. R. Spencer (2004), Geology of Ganymede, in *Jupiter: The Planet, Satellites and Magnetosphere* (Eds. F. Bagenal et al.), Cambridge University Press, Cambridge, United Kingdom.

Passey, Q. R., and E. M. Shoemaker (1982), Craters and basins on Ganymede and Callisto-Morphological indicators of crustal evolution, in *Satellites of Jupiter* (Eds. D. Morrison and M. S. Matthews), University of Arizona Press, Tucson.

Prockter, L. M., G. C. Collins, S. L. Murchie, P. M. Schenk, and R. T. Pappalardo (2002), Ganymede Furrow Systems as Strain Markers: Implications for Evolution and Resurfacing Processes, in *33rd Lunar and Planetary Science Conference*, Abstract

766 #1272, Lunar and Planetary Institute, Houston.
767 Schenk, P. M. (1995), The geology of Callisto, *Journal of Geophysical Research: Planets*,
768 *100*(E9), 19023-19040, doi:10.1029/95JE01855.
769 Schenk, P. M., and F. J. Ridolfi (2002), Morphology and scaling of ejecta deposits on icy
770 satellites, *Geophysical Research Letters*, *29*(12), 1590, doi:10.1029/2001GL013512.
771 Schenk, P. M., and W. B. McKinnon (1987), Ring geometry on Ganymede and Callisto, *Icarus*,
772 *72*(1), 209-234, doi:http://dx.doi.org/10.1016/0019-1035(87)90126-6.
773 Schubert, G., J. Anderson, T. Spohn, and W. McKinnon (2004), Interior composition,
774 structure and dynamics of the Galilean satellites, in *Jupiter: The Planet, Satellites*
775 *and Magnetosphere* (Eds. F. Bagenal et al.), Cambridge University Press, Cambridge,
776 United Kingdom.
777 Senft, L. E., and S. T. Stewart (2008), Impact crater formation in icy layered terrains on
778 Mars, *Meteoritics & Planetary Science*, *43*(12), 1993,
779 doi:doi:10.1111/j.1945-5100.2008.tb00657.x.
780 Shoemaker , E. M., and R. Wolfe (1982), Cratering time scales for the Galilean satellites, in
781 *Satellites of Jupiter* (Eds. D. Morrison and M. S. Matthews), University of Arizona
782 Press, Tucson.
783 Smith, B. A., et al. (1979a), The Galilean Satellites and Jupiter: Voyager 2 Imaging Science
784 Results, *Science*, *206*(4421), 927-950, doi:10.1126/science.206.4421.927.
785 Smith, B. A., et al. (1979b), The Jupiter System Through the Eyes of Voyager 1, *Science*,
786 *204*(4396), 951-972, doi:10.1126/science.204.4396.951.
787 Strom, R. G., A. Woronow, and M. Gurnis (1981), Crater populations on Ganymede and
788 Callisto, *Journal of Geophysical Research: Space Physics*, *86*(A10), 8659-8674,
789 doi:doi:10.1029/JA086iA10p08659.
790 Thompson, S., and H. Lauson (1974), Improvements in the Chart D radiation-hydrodynamic
791 CODE III: Revised analytic equations of state, Sandia National Laboratories Report
792 SC-RR--71-0714, Albuquerque, NM.
793 Tillotson, J. H. (1962), Metallic equations of state for hypervelocity impact, General Atomic
794 Report GA-3216, Division of General Dynamics, John Jay Hopkins Laboratory for
795 Pure and Applied Science, San Diego, CA.
796 Tonks, W. B., and H. Jay Melosh (1992), Core formation by giant impacts, *Icarus*, *100*(2),
797 326-346, doi:https://doi.org/10.1016/0019-1035(92)90104-F.
798 U.S. Geological Survey (2003), Controlled color photomosaic map of Ganymede; Jg 15M
799 CMNK: U.S. Geological Survey Geologic Investigations Series I–2762, available at
800 https://pubs.usgs.gov/imap/i2762/.
801 Wünnemann, K., G. S. Collins, and H. J. Melosh (2006), A strain-based porosity model for

use in hydrocode simulations of impacts and implications for transient crater growth in porous targets, *Icarus*, *180*(2), 514-527, doi:https://doi.org/10.1016/j.icarus.2005.10.013.

Zahnle, K., P. Schenk, H. Levison, and L. Dones (2003), Cratering rates in the outer Solar System, *Icarus*, *163*(2), 263-289.

Zuber, M. T., and E. M. Parmentier (1984), A geometric analysis of surface deformation: Implications for the tectonic evolution of Ganymede, *Icarus*, *60*(1), 200-210, doi:http://dx.doi.org/10.1016/0019-1035(84)90148-9.